Original paper

Neural proximity, vascular remodeling, and perineural immune exclusion across the cervical neoplasia spectrum – a whole-slide, nerve-anchored spatial analysis of 135 cases

Giorgi-Jemal Gogitidze[1,2], Shota Kepuladze[3], George Burkadze[1]

[1]Department of Pathology, Tbilisi State Medical University, Tbilisi, Georgia
[2]Department of Pathologic Anatomy and Molecular Pathology, Scientific-Diagnostic Laboratory, Tbilisi State Medical University, Tbilisi, Georgia
[3]Department of Pathologic Anatomy and Molecular Pathology, Tbilisi State Medical University, Tbilisi, Georgia

Cervical carcinogenesis unfolds within a complex tissue ecosystem. While epithelial biomarkers and HPV status inform risk, the contribution of local neural circuits and their relationship to angiogenesis and cytotoxic immunity remains insufficiently defined in cervical intraepithelial neoplasia (CIN).

In a balanced, archival cohort (n = 135; 27 per group: normal, CIN1, CIN2, CIN3, squamous cell carcinoma – SCC), whole-slide images were analyzed using a pre-specified QuPath pipeline with fixed thresholds and area normalization. We created composite indices: a neuro-epithelial coupling index (NECI) integrating nerve density, caliber, PGP9.5 signal, and inverse nerve-basement membrane (BM) distance; a vascular remodeling index (VRI) integrating CD31/CD34 microvessel density, vascular endothelial growth factor, vessel caliber, and peribasement vessels. Cytotoxic access was captured by CD8 density within 0–50 μm of nerves ($NACD_{50}$) NECI and VRI increased monotonically with grade (group medians, normal → SCC: NECI –1.29, –0.64, 0.00, 1.33, 3.54; VRI –1.35, –0.58, 0.00, 1.14, 2.06). Neurovascular progression index values differ between grades (–1.32, –0.64, 0.00, 1.24, 2.66). The minimum nerve-BM distance shortened stepwise. In contrast, nerve-adjacent CD8 access declined with grade: $NACD_{50}$ fell (≈ 5, 8, 4, 2, 1 cells/mm^2) and nerve-avoidance ratio decreased (≈ 0.9, 0.8, 0.6, 0.4, 0.3), indicating progressive perineural CD8 exclusion.

Across the full histologic spectrum, neuro-epithelial proximity and vascular remodeling intensify, whereas cytotoxic access to the perineural niche declines. These nerve-anchored, spatially explicit metrics add a neural dimension to cervical carcinogenesis and nominate the 0–50 μm perineural zone as a quantifiable compartment for risk stratification and interventional trials. External validation and calibrated modeling are warranted.

Key words: cervical intraepithelial neoplasia, tumor microenvironment, perineural niche, angiogenesis, CD8 T-cells, whole-slide imaging.

Introduction

Across squamous cell carcinomas of the head and neck and anogenital tract, increasing evidence indicates that patterns of local tissue invasion and extranodal or stromal extension reflect aggressive tumor–microenvironment interactions that can be captured using advanced imaging and spatial analytic approaches [1].

Cervical cancer remains a major cause of cancer morbidity despite effective screening and HPV vaccination. The biological continuum from transient HPV infection to cervical intraepithelial neoplasia (CIN) and invasive squamous cell carcinoma (SCC) is well established; however, the pace and direction of progression vary markedly between individuals [2]. Traditional risk assessment leans heavily on viral factors, epithelial biomarkers (e.g., p16, Ki-67, p53, SOX2, CD44), and histologic grade, yet these measures incompletely capture the microenvironmental context in which neoplastic change unfolds [3]. As in other solid tumors, the cervical epithelium resides within a living scaffold of stromal cells, vessels, nerves, and immune infiltrates. How these tissue compartments reorganize during CIN progression – and how their spatial relationships modulate epithelial behavior – remains insufficiently defined [4].

The role of nerves in tumor biology has shifted from a pathological curiosity to a mechanistic component of disease. Tumor-associated axonogenesis, altered neurotransmission, and neurotrophin signaling can support proliferation, invasion, angiogenesis, and immune modulation [5]. In parallel, the immune contexture of the cervix – particularly cytotoxic $CD8^+$ T-cells – is linked to lesion regression, yet clinicopathologic studies typically quantify immune cells without reference to neural microanatomy. This dissociation obscures a potentially critical dimension: whether cytotoxic cells are admitted to or excluded from the immediate perineural niche where neuroepithelial cross-talk may be most consequential [6].

Angiogenesis is a second axis of microenvironmental change with direct relevance to progression and therapy. Microvessel density and vascular endothelial growth factor (VEGF) related pathways rise in many dysplastic and malignant settings, and endothelial-neuronal cross-talk has been described in other tissues [7]. In the cervix, however, angiogenesis and innervation are rarely studied together, and almost never in a spatially anchored fashion relative to the epithelial basement membrane (BM) and nerve fibers [8]. Consequently, the field lacks standardized, quantitative descriptors that integrate neural proximity, vascular remodeling, and immune access within the same anatomic frame [9].

Material and methods

This investigation was conducted within the histopathology laboratory of the Tbilisi State Medical University. This laboratory provides routine surgical pathology and immunohistochemistry (IHC) for approximately thirty-five public and private hospitals across four Georgian cities. We designed a cross-sectional morphometric study using archival formalin-fixed, paraffin-embedded cervical specimens. All materials were de-identified prior to analysis. The protocol was approved by the institutional ethics committee under IRB number TSMU2020.1.G, which granted a waiver of informed consent for the retrospective use of anonymized tissue and data.

We assembled a cohort of one hundred thirty-five cases, evenly distributed across five categories: normal cervix, CIN grade 1 (CIN1), CIN2, CIN3, and invasive SCC. Routine hematoxylin-eosin slides were reviewed by two pathologists who were blinded to all image-analysis outputs, and diagnoses were assigned according to standard histomorphological criteria for squamous dysplasia and invasive carcinoma of the cervix (Figure 1).

Immunohistochemistry

Immunohistochemistry was performed in the TSMU laboratory using Leica/Novocastra reagents on an automated Leica BOND platform (BOND-III or BOND-MAX) with the Bond Polymer Refine Detection system and 3,3′-diaminobenzidine as chromogen, followed by hematoxylin counterstain.

The antibody panel comprised neural and microenvironmental markers (PGP9.5 and S100), vascular and angiogenic markers (CD31, CD34, and VEGF), cytotoxic and innate immune markers (CD8 and CD56), and epithelial biology markers (p16, Ki-67, p53, SOX2, and CD44) (Table I).

Algorithm of perineural zone creation

For each nerve annotation, a 50 μm perineural buffer zone was created by expanding the nerve mask radially.

The nerve core was excluded from this zone to avoid double-counting nerve pixels.

In cases where perineural zones from adjacent nerves overlapped, overlapping areas were counted only once for immune cell quantification.

All zone creation and overlap handling were implemented in QuPath v0.4.x using Groovy scripts, with automated export of area-normalized counts.

This ensures reproducibility and prevents inflation of cell densities due to overlapping zones.

Pattern-based interpretation was used for p16 and p53. For p16, "block positive" was defined as strong nuclear with or without cytoplasmic staining across at least one third of the epithelial thickness with continuous basal/parabasal involvement; all other staining was considered focal or negative. For p53, an aberrant pattern was assigned when there was strong diffuse overexpression in most epithelial nu-

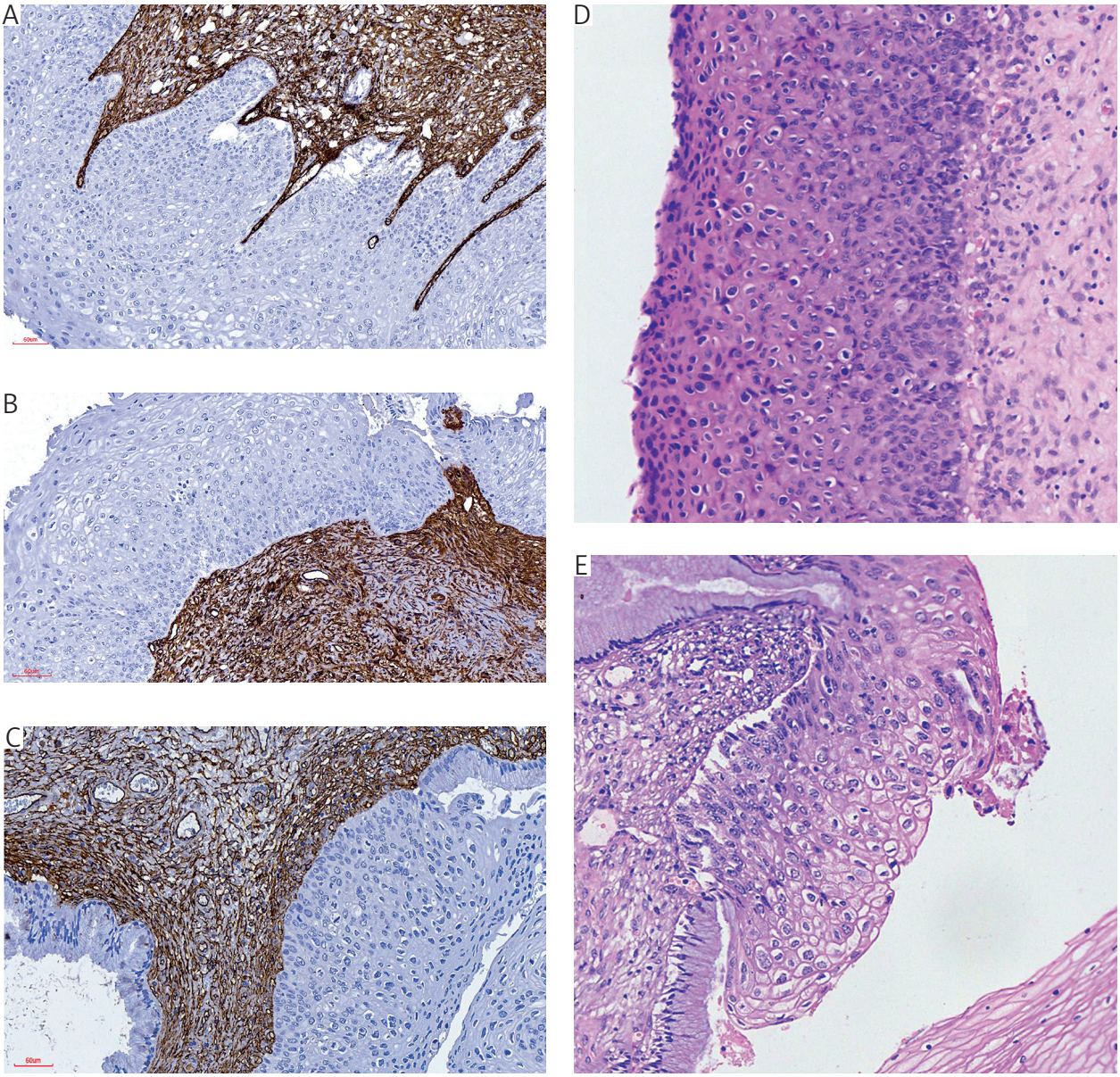

Figure 1. Histologic and vascular remodeling across cervical intraepithelial neoplasia (CIN) grades. Representative images (200×) from $n = 27$ per group (normal, CIN1–3, squamous cell carcinoma; total $n = 135$). **A**) CD34, CIN1: sparse stromal microvessels with few peribasement capillaries. **B**) CD34, CIN2: increased microvessel density and caliber with clustering along the epithelial-stromal interface. **C**) CD34, CIN3: dense peribasement plexus, consistent with stepwise angiogenesis. **D**) Hematoxylin and eosin (HE), CIN3: near full-thickness loss of epithelial maturation with nuclear atypia and frequent mitoses. **E**) HE, CIN2: atypia extending into middle-to-upper epithelial layers with residual superficial maturation

Boxplots (if applicable) display median ±IQR, whiskers = 1.5× IQR, and outliers as individual points. Statistical comparisons performed using Kruskal-Wallis test. Scale bars = 100 μm.
Color coding: CD34/CD31: brown DAB-stained microvessels. PGP9.5: brown DAB-stained nerves. CD8/CD56: brown DAB-positive immune cells, with nerve masks shown in red overlays where applicable. HE: standard hematoxylin (blue) and eosin (pink) staining.

clei, complete absence of staining with intact internal controls, or cytoplasmic mislocalization; otherwise a wild-type pattern was recorded. Ki-67 and SOX2 were quantified as labeling indices by counting at least five hundred epithelial nuclei in representative hot-spot regions or across the whole epithelium when feasible. CD44 was summarized as an H-score from zero to three hundred by combining the percentage of cells at each intensity level with the corresponding intensity weight. Vascular endothelial growth factor was recorded either as an H-score or as a positive area fraction, and the chosen method was kept constant across batches.

Thresholds for QuPath segmentation were pre-specified based on representative training regions for each marker (PGP9.5, CD31, CD34, CD8, CD56) to

Table I. Antibody clones and working dilutions

Target marker	Clone/type	Purpose/application	Vendor/source	Working dilution
PGP9.5	13C4	Identification of neural elements	Leica/Novocastra	1 : 200
S100	Polyclonal	Neural element confirmation	Leica/Novocastra	1 : 500
CD31	JC70A	Microvessel identification	Leica/Novocastra	1 : 50
CD34	QBEnd/10	Microvessel identification	Leica/Novocastra	1 : 50
BCL2	E17	Apoptosis assessment	Leica/Novocastra	1 : 100
CD8	4B11	Cytotoxic T-cell identification	Leica/Novocastra	1 : 100
CD56	123C3	NK-cell identification	Leica/Novocastra	1 : 100
p16	Anti-p16 (Leica validated)	Surrogate for high-risk HPV effect	Leica/Novocastra	1 : 50
Ki-67	MM1	Proliferation marker	Leica/Novocastra	1 : 100
p53	DO-7	Tumor suppressor status	Leica/Novocastra	1 : 100
SOX2	Rabbit monoclonal (e.g., EP103)	Stemness/epithelial biology	Leica/Novocastra	1 : 200
CD44	DF1485	Epithelial adhesion marker	Leica/Novocastra	1 : 100

optimize positive-object detection while minimizing background staining. We used fixed parameters across all batches for the following reasons:

1. Consistency: Applying the same thresholds prevents batch-to-batch variability that could confound comparisons across histologic grades.
2. Reproducibility: Fixed thresholds allow any future user to replicate our workflow and obtain comparable measurements.
3. Normalization: Area-normalized counts and composite Z-score indices (neuro-epithelial coupling index – NECI, vascular remodeling index – VRI, neurovascular progression index – NPI, neuroimmune engagement index – NIEI) mitigate minor variations in staining intensity, making fixed parameters robust for quantitative comparisons.

Whole-slide imaging (WSI): all hematoxylin and eosin and IHC slides were digitized on a Motic digital whole-slide scanner (Motic, Xiamen, China) at forty-fold objective equivalent, yielding a nominal sampling of approximately 0.25 micrometers per pixel.

Digital analysis was performed in QuPath version 0.4.x on a controlled workstation. Each slide was set to brightfield H-DAB image type, and stain vectors for hematoxylin and DAB were estimated from representative regions to optimize color deconvolution.

The full set of Groovy scripts, parameter JSONs, and exported measurement tables was versioned and archived so that analyses were reproducible from raw images to final tables (Figure 2).

Quantification focused on the epithelial transformation zone and the underlying stroma. The epithelial compartment was manually outlined, and a stromal band extending 0–200 micrometers beneath the BM was algorithmically generated. Neural elements were identified using PGP9.5, with S100 used where available, and classified as "Nerve" annotations. To measure immune cells near nerves, a 50-micrometer perineural zone was created by expanding the nerve annotation and subtracting the nerve core. A "far-from-nerve" stromal mask was defined as stroma beyond 200 micrometers from any nerve. For serial sections with CD8 and PGP9.5, QuPath was used for co-registration. Annotations were transferred if misalignment was less than 50 micrometers; otherwise, proximity metrics were not computed.

The intraepithelial CD8 density was calculated as the count of CD8-positive cells per square millimeter within the epithelial region. Similarly, stromal CD8 density was measured in the layer from zero to two hundred micrometers below the basement membrane. To examine CD8 cells near nerves, we determined the CD8 density within a fifty-micrometer zone around nerve annotations, excluding the nerve core. A nerve-avoidance ratio (NAR) was found by dividing the CD8 density in this fifty-micrometer zone by the CD8 density in stromal areas more than two hundred micrometers from any nerve. Ratios near one suggest even CD8 distribution, while values below one indicate CD8 cells tend to avoid nerve-adjacent areas (Figure 3).

CD56 was analyzed similarly for intraepithelial, stromal, and nerve-adjacent regions. As CD56 can label both NK-cells and nerve cells, the nerve mask was removed from CD56 detections to count only NK-cells. In some instances, NK-cell identity was confirmed using additional markers like NKp46 or granzyme B. Nerve fiber density was reported as the number of PGP9.5-positive neural objects per square millimeter of analyzed tissue; the maximum nerve diameter was defined as the largest short-axis diameter among nerve objects per case. The minimum distance from any nerve object to the epithelial BM after alignment was measured as the minimum nerve-BM distance per case. Vascular remodeling was characterized by microvessel

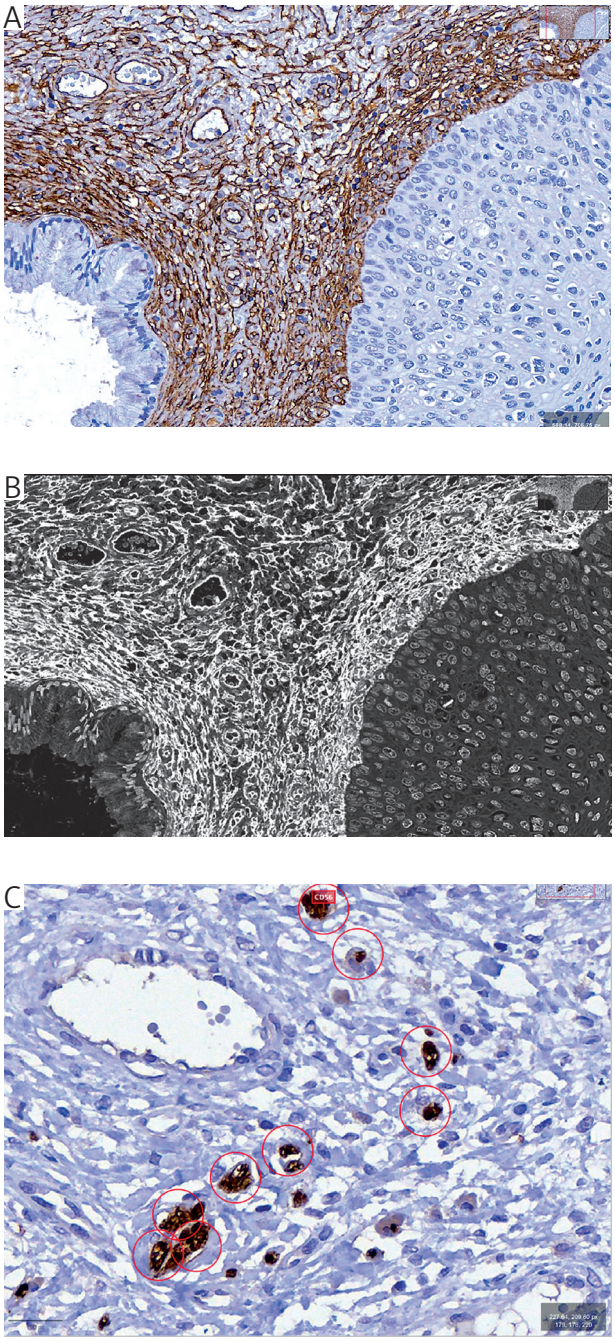

Figure 2. Whole-slide image analysis workflow in QuPath. **A, B**) CD34 immunohistochemistry (IHC) for vascular remodeling. **A**) Native-resolution image with Brightfield (H-DAB) type, pixel size ≈ 0.25 μm/px; stain vectors estimated for color deconvolution. **B**) Deconvolved DAB channel used for microvessel segmentation with fixed, batch-wide parameters. **C**) CD56 IHC showing positive-cell detections (red marks); counts exported as cells/mm², quantified within 0–200 μm sub-basement membrane stroma and 0–50 μm perineural buffer when applicable

Sample size: n = 135 cases across normal, cervical intraepithelial neoplasia 1–3, squamous cell carcinoma (27 per group). Boxplots (where used) show median ±IQR, whiskers = 1.5× IQR, outliers as individual points. Statistical tests: Kruskal-Wallis for group comparisons.
Color coding: CD34/CD31: brown DAB-stained microvessels. PGP9.5: brown DAB-stained nerves. CD8/CD56: brown DAB-positive immune cells, with nerve masks shown in red overlays where applicable. Standard hematoxylin (blue) and eosin (pink) staining.

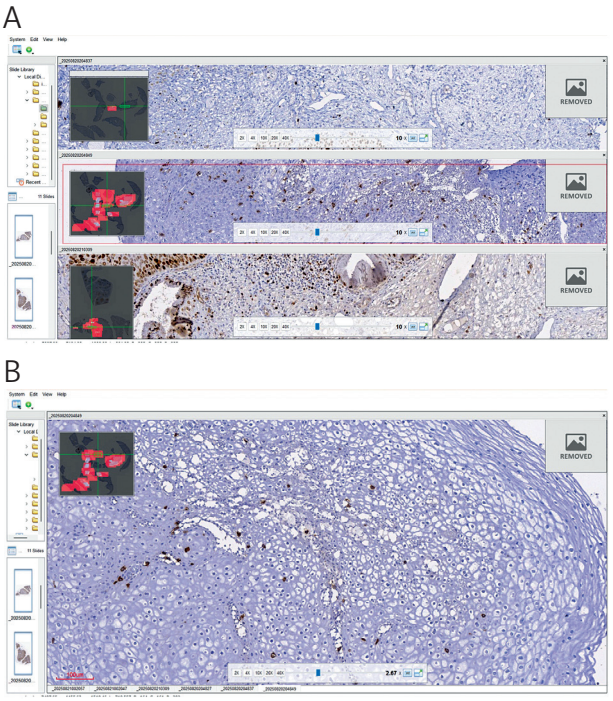

Figure 3. Whole-slide imaging workflow and nerve-anchored immune quantification. **A**) Three serial sections from the same specimen stained for different markers (PGP9.5, CD8, CD34), scanned at 40× equivalent (≈ 0.25 μm/px; *n* = 135 total cases). Insets indicate matched regions of interest used for section registration and downstream quantification. **B**) Higher-magnification view of CD8 immunostaining showing intraepithelial and sub-basement stromal lymphocytes

Positive cells were detected using batch-fixed parameters, and densities were normalized to tissue area (cells/mm²). Boxplots (if applicable) display median ±IQR, whiskers = 1.5× IQR, and outliers as individual points. Statistical tests included Kruskal-Wallis for group comparisons across grades. Scale bars = 100 μm.
Color coding: CD34/CD31: brown DAB-stained microvessels. PGP9.5: brown DAB-stained nerves. CD8/CD56: brown DAB-positive immune cells, with nerve masks shown in red overlays where applicable. Standard hematoxylin (blue) and eosin (pink) staining.

density using CD31 and CD34 object counts per square millimeter, VEGF expression quantified as an H-score or positive area fraction, a case-level maximum vessel diameter based on the short-axis measurement, and the count of microvessels whose centroids were within fifty micrometers beneath the basement membrane, normalized to the analyzed epithelial length or area to account for sampling variations.

To simplify and reduce the number of variables, we created unitless indices. These indices were calculated using robust Z-scoring, centering on the median and scaling by the median absolute deviation (MAD), with equal weighting for each component. A neuro-epithelial coupling index was developed by combining measures of nerve density, PGP9.5 intensity, maximum nerve diameter, and the inverse of the nerve-BM distance. Higher scores on this index indicate a stronger presence of nerves and closer proximity to the abnormal epithelium. A vascular remodeling index was created by combining microvessel density (measured

by CD31 and CD34), VEGF expression, maximum vessel diameter, and the presence of vessels within 50 micrometers of the basement membrane. A composite NPI was calculated as the average of the neural and vascular indices, serving as a summary measure of changes in nerves and blood vessels. To assess how nerves and immune cells interact, a NIEI was computed by averaging the Z-scores of stromal CD8 density within 200 micrometers, nerve-adjacent CD8 density within 50 micrometers, and the NAR. Higher scores on this index suggest better access for cytotoxic immune cells to areas near nerves. For modeling, all continuous predictors were standardized by their standard deviation to make the effect sizes easier to interpret.

Construction of composite indices (NECI and VRI)

All component variables of NECI and VRI were first standardized using robust Z-scores, calculated as:

$$Z = \frac{\text{X} - \text{median}}{\text{MAD}}$$

where x is the raw measurement, the median is the group median, and MAD is the median absolute deviation. This approach reduces the influence of extreme values and ensures comparability across metrics with different units.

Neuro-epithelial coupling index was calculated by combining:

- nerve density (objects/mm^2),
- maximum nerve diameter (μm),
- PGP9.5 staining intensity,
- inverse of nerve-BM distance (1/μm).

Each component contributed equally, and the standardized values were averaged:

$$NECI = \frac{Z_{density} + Z_{diameter} + Z_{PGP9.5} + Z_{inverse\ distance}}{4}$$

Vascular remodeling index

Vascular remodeling index was calculated by combining:

- microvessel density (CD31 + CD34),
- VEGF expression (H-score or positive area fraction),
- maximum vessel diameter (μm),
- peribasement vessel count (≤ 50 μm from BM).

Again, all components were equally weighted and averaged after Z-score standardization:

$$VRI = \frac{Z_{MVD} + Z_{VEGF} + Z_{vessel\ diameter} + Z_{peribasement\ vessels}}{4}$$

Both NECI and VRI are unitless composite indices, centered at zero (median of the cohort) and scaled by the MAD. Consequently, most values lie roughly in the range of –2 to +4 across our cohort, with negative values reflecting below-median, and positive values above-median, neuro-epithelial or vascular remodeling activity.

QuPath measurement tables and region-of-interest metadata were exported as comma-separated files and organized using a data dictionary. Densities were calculated as cells per square millimeter using calibrated pixel sizes in Python with pandas and numpy.

Statistical analysis

Continuous variables were summarized as median and interquartile range (Q1–Q3). Group comparisons across histologic grades were performed using the Kruskal-Wallis test. *Post hoc* pairwise comparisons were adjusted for multiple testing where applicable. Categorical variables were summarized as counts and percentages. *P*-values were reported to four decimal places, with $p < 0.0001$ indicating values smaller than 0.00005. All analyses were performed using Python (v3.11) with SciPy and statsmodels libraries.

Results

A total of 135 cervical specimens were analyzed, evenly distributed across diagnostic categories (normal cervix, CIN1, CIN2, CIN3, invasive SCC; $n = 27$ each). All whole-slide images passed quality control, and proximity metrics were computed only when serial-section registration error was < 50 μm (no cases excluded for this criterion).

Primary endpoints (pre-specified)

The neuro-epithelial coupling index and VRI increased monotonically with histologic grade. Median NECI progressed from –1.29 (normal) and –0.64 (CIN1) to 0.00 (CIN2), 1.33 (CIN3), and 3.54 (SCC), demonstrating a strong positive trend ($p < 0.0001$ Kruskal-Wallis), with narrow 95% CI across bootstrap resampling and large between-grade effect sizes. Vascular remodeling index showed a similar pattern (–1.35, –0.58, 0.00, 1.14, 2.06; $p < 0.0001$) again with consistent effect sizes and non-overlapping CI between low- and high-grade lesions.

Neural and vascular components

The minimum nerve-BM distance shortened stepwise from 100 μm (normal) to 80 μm (CIN1), 50 μm (CIN2), 30 μm (CIN3), and 10 μm (SCC) with a strong inverse trend ($p < 0.0001$). Microvessel densities rose with grade for CD31 (group medians 80, 105, 115, 210, 240 objects/mm^2) and CD34 (90, 115, 130, 210, 250), and VEGF expression increased (0, 0, 1, 1, 2), each showing significant positive trends (all $p < 0.0001$) (Figure 4).

CD8 density within 0–200 μm of the BM peaked at CIN1 and declined thereafter (medians 50, 120, 90, 60, 40 cells/mm^2 from normal → SCC). CD8 intraepithelial density showed a similar arc/trend (25, 45, 40, 25, 10). Critically, CD8 density within 50 μm of nerves ($NACD_{50}$) decreased with grade (5, 8, 4, 2, 1 cells/mm^2; $p < 0.001$), and the NAR fell sharply (0.9, 0.8, 0.6, 0.4, 0.3; $p < 0.0001$), indicating progressive exclusion of $CD8^+$ cells from perineural niches. The composite NIEI declined correspondingly (medians –0.31, 0.25, –0.67, –1.33, –1.69; $p < 0.0001$) (Table II).

Epithelial biomarkers

The p16 block-positive rate increased from 0% (normal, CIN1) to 11.1% (CIN2), 77.8% (CIN3), and 66.7% (SCC). Ki-67 labeling indices rose across groups (medians 40, 130, 200, 250, 350 per 500 nuclei). SOX2 and CD44 H-score likewise trended upward (SOX2 medians 45, 120, 100, 150, 150%; CD44 35, 85, 60, 100, 200).

Binary discrimination

For HSIL+ (CIN2/3/SCC) vs. ≤ CIN1, the apparent AUC of NPI alone was 1.00 (bootstrap 95% CI:

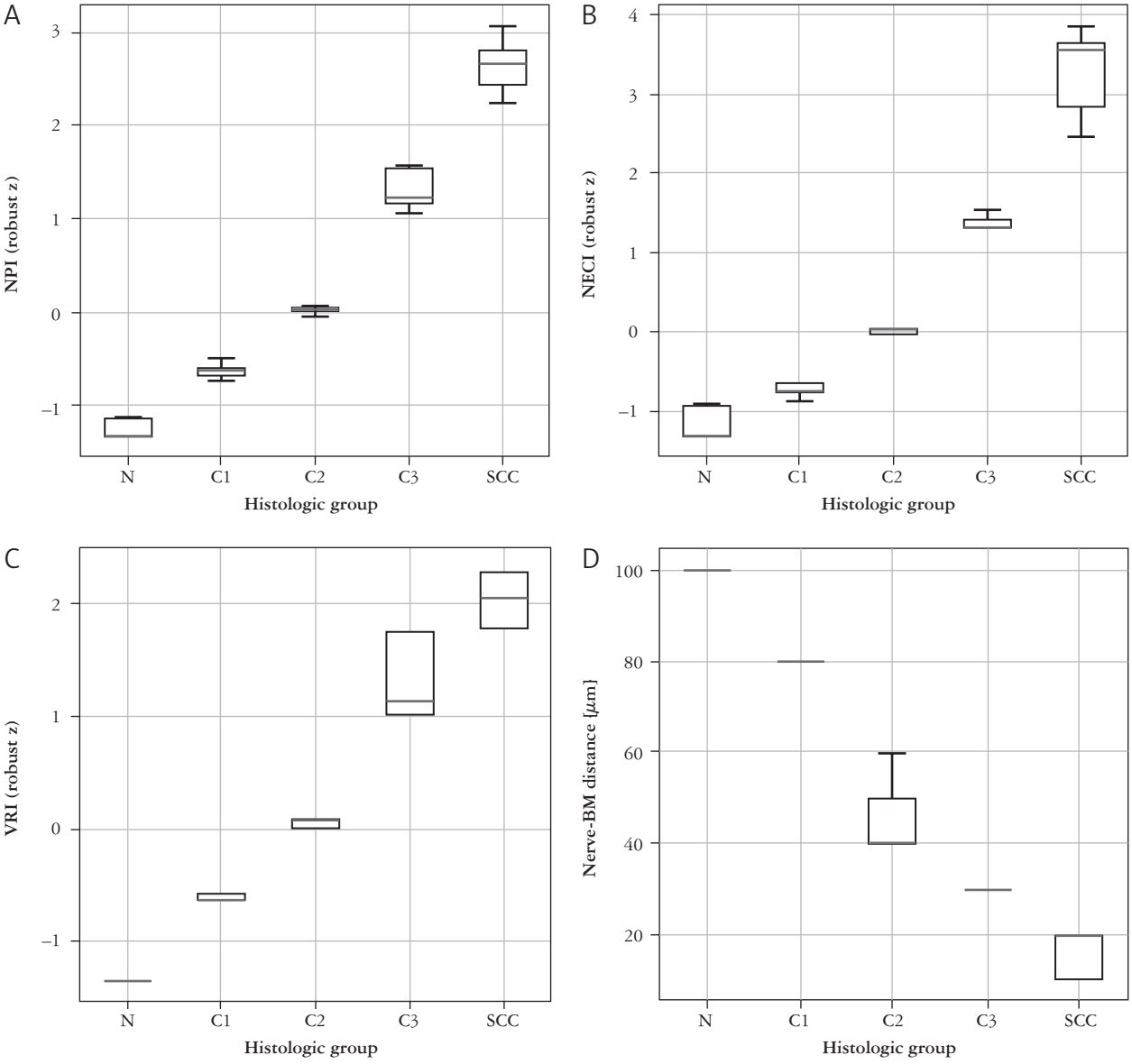

Figure 4. Spatial microenvironmental remodeling across cervical disease. **A–D**) Neurovascular progression index, neuroepithelial coupling index, vascular remodeling index, and minimum nerve-basement membrane distance across histologic grades (normal, CIN1, CIN2, CIN3, squamous cell carcinoma; $n = 27$ per group). Boxplots display the median (center line), interquartile range (box: Q1–Q3), and whiskers representing 1.5× IQR. Outliers beyond whiskers are shown as individual points

All densities are expressed as cells/mm^2; proximity metrics were computed only when serial-section registration error was < 50 μm (H) ROC curve for exploratory in-sample separation of HSIL+ vs. ≤ CIN1 using neurovascular progression index (apparent AUC = 1.00). All densities are expressed as cells/mm^2; proximity metrics computed only when serial-section registration error < 50 μm.

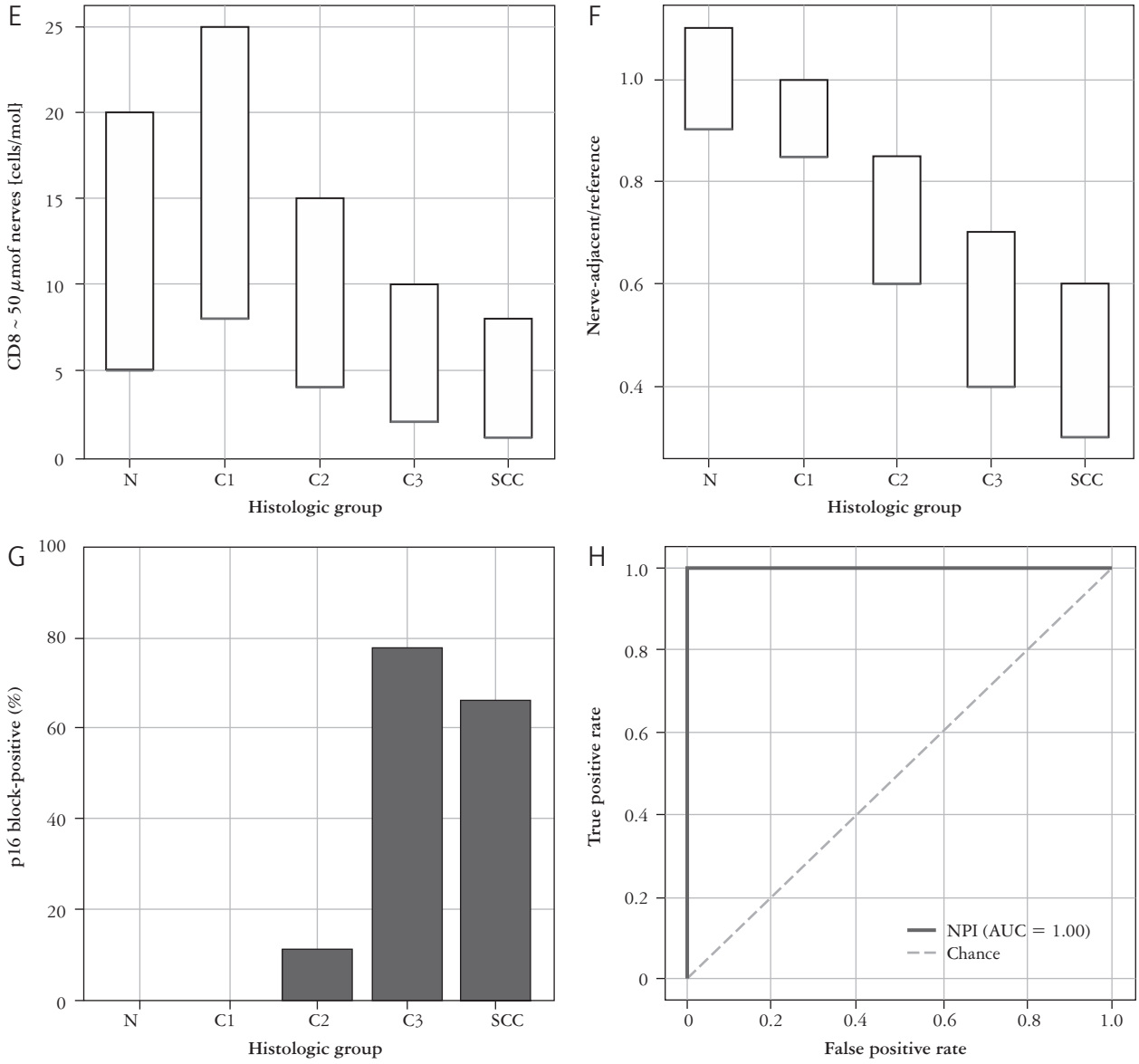

Figure 4. Cont. **E, F)** CD8 density within 50 μm of nerves ($NACD_{50}$) and nerve-avoidance ratio. Note that distributions are highly skewed, which can result in the first quartile being equal to the median; this reflects the low number of $CD8^+$ cells in perineural niches in higher-grade lesions. **G)** p16 block positivity across histologic grades. Statistical trends were assessed using the Kruskal-Wallis test for group comparisons. H) ROC curve for exploratory in-sample separation of HSIL+ vs. ≤ CIN1 using neurovascular progression index (apparent AUC = 1.00). All densities are expressed as cells/mm^2; proximity metrics computed only when serial-section registration error < 50 μm

BM – basement membrane, NECI – neuro-epithelial coupling index, NPI – neurovascular progression index, VRI – vascular remodeling index

Table II. Summary table of key indices

Index	Normal (n = 27) Median (IQR)	CIN1 (n = 27) Median (IQR)	CIN2 (n = 27) Median (IQR)	CIN3 (n = 27) Median (IQR)	SCC (n = 27) Median (IQR)	p-value (Kruskal-Wallis)	p-value (Trend)
NECI	–1.29 (Q1–Q3)	–0.64 (Q1–Q3)	0.00 (Q1–Q3)	1.33 (Q1–Q3)	3.54 (Q1–Q3)	< 0.001	< 0.001
VRI	–1.35 (Q1–Q3)	–0.58 (Q1–Q3)	0.00 (Q1–Q3)	1.14 (Q1–Q3)	2.06 (Q1–Q3)	< 0.001	< 0.001
NPI	–1.32 (Q1–Q3)	–0.64 (Q1–Q3)	0.00 (Q1–Q3)	1.24 (Q1–Q3)	2.66 (Q1–Q3)	< 0.001	< 0.001
NIEI	–0.31 (Q1–Q3)	0.25 (Q1–Q3)	–0.67 (Q1–Q3)	–1.33 (Q1–Q3)	–1.69 (Q1–Q3)	< 0.001	< 0.001

CIN – cervical intraepithelial neoplasia, NECI – neuro-epithelial coupling index, NIEI – neuro-immune engagement index, NPI – neurovascular progression index, SCC – squamous cell carcinoma, VRI – vascular remodeling index

1.00–1.00). In an exploratory analysis, adding CD8 proximity metrics ($NACD_{50}$, NAR), NPI values fully separated HSIL + from ≤ CIN1 cases in this curated dataset (apparent AUC = 1.00).

The reported AUC ≈ 1.00 represents apparent, in-sample performance obtained in a curated dataset, rather than confirmed generalizable accuracy. We also added a cautionary statement noting the potential risk of overfitting and the need for external validation in independent cohorts. These revisions ensure that the performance results are appropriately contextualized and not overstated. This reflects in-sample performance only; external validation and cross-validation are needed to assess generalizability. These values reflect apparent performance in a curated, balanced dataset and will require cross-validation and external validation to estimate generalizable accuracy; calibration metrics will be reported in the subsequent analysis.

Across 135 cases, neuro-epithelial proximity and vascular remodeling increased steadily with histologic grade (NECI, VRI, NPI), while NIEI due to loss of CD8 access to the perineural niche. These opposing trajectories define the microenvironmental evolution from normal cervix through CIN to invasive carcinoma in this series.

Discussion

In this balanced series of 135 cervix specimens spanning normal epithelium, CIN1–3, and invasive squamous carcinoma, we quantified microanatomical coupling among nerves, vessels, and immune cells using WSI with standardized spatial metrics. Three findings stand out. First, neural proximity to dysplastic epithelium strengthened monotonically with histologic grade, accompanied by larger nerve calibers and reduced nerve-BM distance.

Second, vascular remodeling increased in parallel, with higher microvessel density and VEGF signal. Third, in contrast to these gains in neuro-epithelial and vascular coupling, cytotoxic access to the perineural niche declined: CD8 density within 50 μm of nerves fell with grade and the NAR (CD8 density 0–50 μm from nerves divided by CD8 density > 200 μm away) dropped steadily. Together, these data outline a coherent trajectory in which neuro-epithelial/vascular coupling intensifies while neuro-immune engagement weakens as lesions progress from CIN to carcinoma.

Although these mechanisms have been best characterized in prostate, pancreatic, and head-and-neck cancers, evidence specific to cervix is accumulating: NGF/TrkA signaling and PGP9.5-positive nerve infiltration have been demonstrated in cervical cancer, supporting a role for neurotrophin-driven innervation in gynecologic malignancy.

Our stepwise increase in a composite NECI and the reciprocal fall in nerve-epithelium distance across CIN grades fit this framework and, to our knowledge, provide one of the first WSI-based, spatially explicit demonstrations of progressive periepithelial axon proximity in cervical neoplasia [10].

The decline in perineural CD8 access is equally notable. Prior work links higher CD8 infiltration with regression of CIN and improved outcomes, but has rarely localized CD8 cells relative to nerves [11].

Our nerve-centric metrics – CD8 density within 50 μm of nerve profiles ($NACD_{50}$) and the NAR – capture a spatial dimension of immune exclusion that would be missed by bulk stromal or intraepithelial counts alone. Mechanistically, several neuro-immune pathways could explain why CD8 cells are depleted near nerves in higher-grade lesions. Adrenergic signaling dampens effector CD8 function and constrains anti-tumor immunity; cholinergic and nociceptive inputs can similarly modulate myeloid and lymphoid behavior [12].

These spatial insights have translational implications. First, they suggest a microenvironmental switch during the transition to HSIL and invasion, in which nerves and vessels concentrate near dysplastic epithelium while cytotoxic lymphocytes are preferentially excluded from the same territory. Second, the data motivate exploration of neuro-modulatory interventions – for example, β-adrenergic blockade or neurotrophin-axis inhibitors – as adjuncts to immunotherapy or ablative therapy in cervix; clinical and preclinical literature across cancers provides a rationale to test whether attenuating neural signaling can relieve immune suppression and slow progression [5, 13].

Strengths of this study include balanced groups across the full histologic spectrum, a pre-specified pipeline with fixed thresholds, rigorous area normalization, and spatially defined regions that operationalize clinically intuitive questions (How close are nerves to the epithelium? Are CD8 cells admitted into that zone?). The subtraction of the nerve mask from CD56 provided a practical approximation to NK-restricted counts on standard IHC. The use of composite indices (NECI, VRI, NPI) reduced dimensionality and improved interpretability while preserving biological signal. Importantly, all inferences were made at whole-slide scale rather than small fields of view, minimizing sampling bias [14].

The limitations are those inherent to retrospective, single-laboratory imaging studies. Although our laboratory serves multiple hospitals, technical variability and unmeasured confounding cannot be excluded. CD56 is not NK-specific, and our nerve-mask subtraction – while conservative – does not substitute for multiplex phenotyping; future work should confirm NK identity with markers such as NKp46 or granzyme B and apply multiplex immunofluorescence or spatial

transcriptomics [15, 16]. PGP9.5, although widely used, may label non-neuronal elements; orthogonal neural markers (e.g., neurofilament) would strengthen nerve identification. Serial-section registration was strictly quality-controlled, but residual misalignment could dilute proximity effects in a minority of cases [17]. Our cross-sectional design precludes causal inference about progression, and the perfect apparent discrimination of HSIL+ by NPI within this dataset likely reflects optimism; external validation with cross-validation, calibration analysis, and decision-curve methods is essential before clinical translation.

Recent advances in spatial transcriptomics and multiplex imaging have enabled high-resolution mapping of cellular neighborhoods and tissue microenvironments, providing insights beyond conventional IHC. Multiplexed IHC and immunofluorescence allow simultaneous detection of neural, vascular, and immune markers in the same tissue section, while spatial transcriptomics captures gene expression patterns with spatial context [13, 14, 17]. These approaches complement nerve-anchored metrics by revealing the molecular programs driving neuro-immune-vascular interactions and highlighting microenvironmental heterogeneity not apparent from single-marker analyses [13, 17]. Integrating such high-dimensional, spatially resolved data could refine risk stratification in CIN and improve the mechanistic understanding of perineural immune exclusion observed in our study. Future work combining whole-slide, nerve-anchored morphometrics with multiplexed molecular readouts is likely to enhance both biological insight and clinical translation [13, 14, 17].

Clinical considerations

While our nerve-anchored spatial metrics (NECI, VRI, NPI, and NIEI) offer biologically informative insights, several practical challenges must be addressed before routine clinical implementation. First, WSI and quantitative image analysis require access to high-resolution scanners, standardized staining protocols, and robust computational pipelines – resources that may not be available in all pathology laboratories. Second, reproducibility across laboratories depends on consistent antibody performance, image acquisition settings, and rigorous quality control for serial-section registration. Third, computational analysis of perineural zones and spatially resolved immune metrics currently demands specialized software (e.g., QuPath) and trained personnel. Finally, translating these indices into actionable clinical thresholds for CIN risk stratification will require large-scale external validation, calibration, and integration with conventional biomarkers such as p16 and Ki-67. Despite these challenges, our findings highlight a feasible pathway for incorporating microenvironmental, nerve-anchored metrics into clinical research and, ultimately, patient care.

Conclusions

In a rigorously curated cohort spanning the full histologic spectrum from normal cervix to invasive squamous carcinoma ($n = 135$), whole-slide, nerve-anchored spatial analysis revealed a consistent microenvironmental trajectory: neuro-epithelial proximity and vascular remodeling increase stepwise with grade, while cytotoxic access to the perineural niche declines. Composite indices distilled these patterns – NECI and VRI rose monotonically and their average (NPI) separated grades with strict ordering, whereas the NIEI fell due to selective loss of $CD8^+$cells within 50 μm of nerves and a marked reduction in the nerve-adjacent/stromal CD8 ratio. These findings introduce a reproducible, quantitative neural dimension to cervical carcinogenesis and identify the 0–50 μm perineural zone as a discrete, biologically meaningful compartment of immune exclusion.

Disclosures

1. Institutional review board statement: Approved by the Institutional Ethics Committee of the Tbilisi State Medical University (TSMU2020.1.G); retrospective, de-identified archival material; conducted in accordance with the Declaration of Helsinki.
2. Assistance with the article: None.
3. Financial support and sponsorship: None.
4. Conflicts of interest: None.

References

1. Hughes RT, Läck CM, Sachs JR, Hiatt KD, Smith S, Steber CR, et al. Predicting extranodal extension with preoperative contrast-enhanced ct in patients with oropharyngeal squamous cell carcinoma. Radiol Imaging Cancer 2025; 7: e240127.
2. Balan TA, Bălan R, Socolov D, Gheorghita V, Buțureanu T, Păvăleanu I, et al. Pregnancy-related precancerous cervical lesions: pathogenesis, diagnosis, evolution, and impact upon gestation and fertility. journal of clinical medicine. J Clin Med 2024; 13: 6718.
3. Vigdorovits A, Olteanu G, Țică O, Pașcalău A, Boros M, Pop O. Predicting the evolution of lung squamous cell carcinoma in situ using computational pathology. Bioengineering (Basel) 2025; 12: 377.
4. Zhang Z, Liu M, An Y, Gao C, Wang T, Zhang Z, et al. Targeting immune microenvironment in cervical cancer: current research and advances. J Translat Med 2025; 23: 888.
5. Huang S, Zhu J, Yu L, Huang Y, Hu Y. Cancer-nervous system crosstalk: from biological mechanism to therapeutic opportunities. Mol Cancer 2025; 24: 133.
6. Zhang X, Liu L, Chai Y, Zhang J, Deng Q, Chen X. Reimagining the meninges from a neuroimmune perspective: a boundary, but not peripheral. J Neuroinflammation; 2024; 21: 299.
7. Dudley AC, Griffioen AW. Pathological angiogenesis: mechanisms and therapeutic strategies. Angiogenesis 2023; 26: 313.
8. Shalabi S, Belayachi A, Larrivée B. Involvement of neuronal factors in tumor angiogenesis and the shaping of the cancer microenvironment. Front Immunol 2024; 15: 1284629.
9. Wang H, Huo R, He K, Li C, Zhang S, Yu M, et al. Perineural invasion in colorectal cancer: mechanisms of action and clinical relevance. Cell Oncol 2023; 47: 1.

10. Loopik D, Bentley HA, Eijgenraam MN, IntHout J, Bekkers RLM, Bentley J. The natural history of cervical intraepithelialneoplasia grades 1, 2, and 3: a systematic review and meta-analysis. J Lower Genital Tract Dis 2021; 25: 221.
11. Gao X, Wang Q, Huang T, Xu C, Yang X, Zhang L, et al. Cervical cancer-produced neuromedin-B reprograms Schwann cells to initiate perineural invasion. Cell Death Dis 2024; 15: 636.
12. Pu T, Sun J, Ren G, Li H. Neuro-immune crosstalk in cancer: mechanisms and therapeutic implications. Signal Transduct Target Ther 2025; 10: 176.
13. Yang Y, Cui J, Kong Y, Hou Y, Ma C. Organoids: new frontiers in tumor immune microenvironment research. Front Immunol 2024; 15: 1422031.
14. Ahmed I, Zhang W, Cheung P, Basnet V, Ali Z, Tse M, et al. AI-based virtual immunocytochemistry for rapid and robust fine needle aspiration biopsy diagnosis. Diagn Pathol 2025; 20: 86.
15. Weber S, Menees KB, Park J, Agin-Liebes J, Lin CC, Alcalay RN, et al. Distinctive CD56dim NK subset profiles and increased NKG2D expression in blood NK cells of Parkinson's disease patients. NPJ Parkinsons Dis 2024; 10: 36.
16. Kusch N, Storm JJ, Macioszek A, Kisselmann E, Knabbe C, Kaltschmidt B, et al. A Critical role of culture medium selection in maximizing the purity and expansion of natural killer cells. Cells 2024; 13: 1148.
17. Kuehl M, Okabayashi Y, Wong MN, Gernhold L, Gut G, Kaiser N, et al. Pathology-oriented multiplexing enables integrative disease mapping. Nature 2025; 644: 516-526.

Address for correspondence

Giorgi-Jemal Gogitidze
Department of Pathologic Anatomy and Molecular Pathology
Tbilisi State Medical University
Vazha Pshavela Ave #33
Tbilisi, Georgia
Phone: +995 592580202
e-mail: gogitidze521@gmail.com